

Research Article

Experimental Investigations of the Process of Carbonate Fracture Dissolution Enlargement under Reservoir Temperature and Pressure Conditions

Jingxia Wang and Qingchun Yu 

Beijing Key Laboratory of Water Resources & Environmental Engineering, China University of Geosciences (Beijing), Beijing 10083, China

Correspondence should be addressed to Qingchun Yu; yuqch@cugb.edu.cn

Received 8 May 2018; Accepted 24 July 2018; Published 12 September 2018

Academic Editor: Mercè Corbella

Copyright © 2018 Jingxia Wang and Qingchun Yu. This is an open access article distributed under the Creative Commons Attribution License, which permits unrestricted use, distribution, and reproduction in any medium, provided the original work is properly cited.

Karst is a central focus in the field of carbonate reservoir geology. Fracture dissolution enlargement is an important mechanism for the formation of high-quality reservoirs. This study performed four carbonate fracture dissolution enlargement (CFDE) experiments under a confining pressure of 20 MPa, and temperatures ranged from 40 to 60°C. CO₂-saturated deionized water was injected into artificial carbonate fractures at approximately 11.5 ml/h for 96, 208, 216, and 216 hours. The water flowing out of the fractures was sampled every 8 h to monitor the concentration of Ca²⁺. SEM photomicrographs and 3D laser scanning images were taken before and after the CFDE experiments to observe the dissolution process of the fracture surfaces. After the CFDE experiment, the hydraulic apertures (B_h) of sample 1 (S_1), sample 3 (S_3), and sample 4 (S_4) were enlarged by 3.4, 1.4, and 1.2 times, respectively. The aperture of sample 2 (S_2) was slightly reduced in the early stage of the experiment. The experimental results of this study demonstrate that B_h can be divided into three categories as a function of time: S type, logarithmic type, and polynomial type. The laboratory dissolution rate of S_1 , S_2 , S_3 , and S_4 were 2.50×10^{-6} , 3.11×10^{-6} , 2.70×10^{-6} , and 3.04×10^{-6} mol/m²/s. The pattern of fracture dissolution is closely related to the Peclet and Damkohler numbers. The dissolution processes of high Peclet and Damkohler numbers lead to a pattern of obvious channelization. The Peclet and Damkohler numbers of the S_3 CFDE experiment were the highest, and the channelizing dissolution is the most notable in S_3 of the four fractures. A dissolution process at low temperature has a higher Peclet number and thus leads to obvious channelizing dissolution. Mineral heterogeneities in the rock also play a significant role in channelizing dissolution. A preferential channel typically develops in places where bioclasts are accumulated or the calcite veins are distributed.

1. Introduction

Karst is one of the central focuses in the field of carbonate reservoir geology and has attracted considerable attention from scientists worldwide [1–8]. Carbonate fractures play an important role in oil and gas transport and storage. Fracture dissolution, which can create massive pores, is a common mechanism for the formation of high-quality carbonate reservoirs.

Many carbonate rock dissolution studies have been conducted over the last few decades. Many studies investigating

the kinetics of carbonate dissolution have been published (e.g., [9–16]). Durham et al. [17] suggested that the flow of CO₂-saturated water in carbonate fractures under atmospheric pressure and temperature typically leads to a single broad channel along the flow direction. Dissolution experiments in transparent analog fractures at small confining stress (0.2 MPa) indicated evidence of the preferential dissolution of small apertures surrounding contacting asperities and brittle failure of asperities [18]. The apparent activation energy is an important parameter for characterizing the dissolution reaction kinetics. Plummer et al. [12] found that

TABLE 1: Lithology, length, depth, and mineralogical composition of the carbonate samples.

Sample	Lithology	Length (cm)	Depth (m)	Calcite	Quartz	Ankerite	Clay	Pyrite
S ₁	Bioclastic limestone	8.120	285.75	98.9%			0.7%	0.4%
S ₂	Microcrystalline limestone	8.490	137.52	92.8%	4%	2%	0.6%	0.6%
S ₃	Microcrystalline limestone	6.010	302.22	96.8%	2%		0.7%	0.5%
S ₄	Bioclastic limestone	6.130	106.80	86.8%	4%	8%	0.5%	0.7%

TABLE 2: Chemical composition of the carbonate samples. Major oxides (wt.%).

Sample	CaO	MgO	SiO ₂	Fe ₂ O ₃	TiO ₂	Al ₂ O ₃	MnO	K ₂ O	P ₂ O ₅	S	LOI
S ₁	54.05	0.408	1.47	0.407	0.025	1.0	0.408	0.137	0.019	0.059	42.01
S ₂	51.66	0.794	3.96	1.14	0.029	0.816	0.087	0.066	0.032	0.156	41.08
S ₃	54.3	0.472	1.13	0.345		0.09	0.035	0.008	0.042	0.04	43.40
S ₄	48.29	1.35	6.34	1.57	0.016	0.599	0.153	0.021	0.014	0.034	41.54

the activation energy is temperature-dependent. The activation energy is 6.4 kJ/mol when the temperature is below 25°C and may increase to as high as 33.1 kJ/mol at higher temperatures. The CO₂-promoted dissolution had an activation energy of 41.8 kJ/mol. For far-from-equilibrium diluted solutions, the activation energies range from 43 to 48 kJ/mol [13, 19]. Kirstein et al. [20] demonstrated that care must be taken when obtaining laboratory dissolution rate data from experimental fracture carbonate and when using these rates and activation energies to predict the natural fracture carbonate dissolution rate and fracture channelization systems.

The Qaidam Basin is an important oil and gas basin in Western China. The temperature of the basin ranges from 30 to 60°C [21]. A geological survey indicated that the low permeability limestone in the Qaidam Basin may include oil and gas reservoirs [22, 23]. This limestone contains large amounts of fractures, which serve as conduits for water, oil, and gas. In these conduits, the long-lasting flow of fluids in disequilibrium with the rock is expected. Dissolution processes can alter the geometry of fractures and thus their hydraulic and transport properties [24]. The impact of heterogeneities on the evolution of permeability and dissolution patterns of carbonate fracture media has been evaluated [25–27]. The evolution of fracture structures is directly related to the fluid flow and mineral dissolution rates. Feedback between the fluid flow, solute transport, and mineral dissolution may lead to the formation of preferential flow channels (wormholes) under certain flow and reactivity conditions [28]. Experimental studies of dissolution patterns in a single rock fracture [17, 18, 29–32] have been conducted, but the physicochemical mechanisms behind pattern formation (e.g., the influences of temperature and fracture surface heterogeneities) remain unclear.

At present, there are few studies on the dissolution enlargement process of the carbonate fractures under reservoir temperature and pressure conditions. Moreover, the investigation of dissolution enlargement in carbonate fractured reservoirs has been demonstrated to hold practical and theoretical significance for predicting reservoir spatial

evolution. Therefore, in our study, four carbonate core samples were collected from the Carboniferous Keluke Formation in the Qaidam Basin. The four carbonate core samples were artificially fractured to perform the carbonate fracture dissolution enlargement (CFDE) experiments. The hydraulic aperture (B_h) and dissolution aperture (B_d) at different moments were calculated, and the variations in B_h and B_d over time were analyzed to investigate the process of dissolution. The experimental results of this study demonstrate that the temperature affects the Peclet and Damkohler numbers, dissolution rate, and dissolution pattern. The relationship between the dissolution pattern and temperature is discussed. SEM photomicrographs and 3D laser scanning images were taken before and after the CFDE experiments to determine the locations of the channels and the mineral particles affected by preferential dissolution.

2. Materials and Methods

2.1. Sample Characterization. Four carbonate core samples were collected from the Carboniferous Keluke Formation in the Qaidam Basin. Two samples were extracted from the number 1 borehole, and the other two samples were extracted from the number 2 borehole. The two boreholes are located in the Shihuigou area of the eastern Qaidam Basin. These four samples are referred to as S₁, S₂, S₃, and S₄ in this study. The chemical and mineralogical compositions of the samples were determined at the Micro-Structure Analytical Laboratory of Beijing University. A Thermo Electron Corporation ARL Advant XP⁺ X-ray fluorescence spectrometer was used to analyze the chemical composition of the samples, and a Rigaku D/Max-RA X-ray diffractometer was used to analyze the mineral composition. Tables 1 and 2 show the mineralogical and chemical composition of the samples, respectively.

We conducted a seepage experiment when the confining and back pressures were set to 20.00 MPa and 8.00 MPa, respectively. After three months, no water passes through the carbonate core. Thus, the matrix flow can be ignored.

The four cylindrical carbonate samples were artificially fractured using a wire saw, and the longitudinal fractures

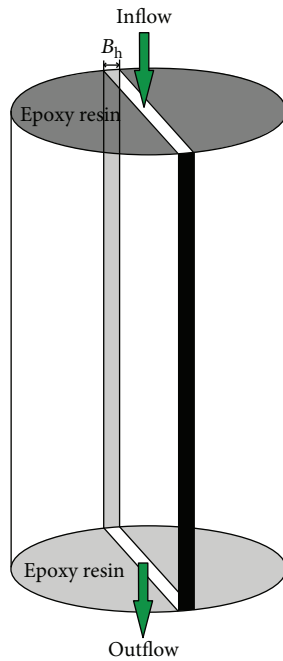


FIGURE 1: Schematic diagram of the carbonate samples after having been fractured and covered by epoxy resin.

were parallel to the cylinder axis. The two fracture walls of each sample were combined and sealed with epoxy resin (stable mechanical and chemical properties up to 690 bar, 260°C, and low pH) on their edges to prevent any mechanical displacement of the fracture walls. The external surfaces of the carbonate fractured samples apart from the fracture inlet and outlet were also covered with epoxy resin to avoid dissolution (Figure 1). These fractured carbonate samples were then inserted into heat-shrinkable tubes to prevent possible crushing of each half from the seam line, after which they were placed into the core holder for the CFDE experiments.

2.2. Experimental Apparatus. Figure 2 shows the experimental apparatus used in the CFDE experiments. The experimental apparatus consists of 6 subsystems: (1) a gas pressurization system was used for gaseous CO_2 pressurization reaching 20 MPa. After pressurization, CO_2 is stored in the gas container. (2) A gas injection system was used to inject CO_2 into the liquid container at a constant pressure (8 MPa) for 12 h. The outlet valve (I) of the gas container can be adjusted to control the gas pressure of the CO_2 gas injected into the liquid container. (3) A liquid injection system was used to inject liquid into the core holder using a piston pump at a controlled flow rate of approximately 11.5 ml/h. (4) The core clamping system is composed of a core holder. The rock core is wrapped in a fluororubber sleeve, placed inside the stainless-steel core holder, and then placed horizontally in a thermostatically controlled chamber. The fluororubber sleeve is highly elastic and acid-resistant. (5) A confining and back pressure system was used. The back pressure system uses a syringe pump to control the initial pressure within the core. Fluid can flow out of the core fracture only when the fluid pressure exceeds the preset back pressure.

The confining pressure, set to 20 MPa for all of the dissolution experiments, was also applied around the rock core using the syringe pump. The confining pressure was always higher than the axial pressure. (6) The measuring system includes two pressure gauges at the inlet and outlet of the core holder and an electronic scale to weigh the water cumulatively collected in the liquid tank at the outlet.

As shown in Figure 2, the liquid containers, the gas and liquid injection valves, the core holder, the two valves on the core holder, and the pipe lines are all temperature-controlled with a thermostat. The portions of the system under temperature control are surrounded by the dashed gray lines in Figure 2. In every experiment, both the pressures and volumetric flow rates were recorded every 30 s.

2.3. Experimental Approach. A sample was installed in the core holder, and the confining and back pressures were set to 20.00 MPa and 8.00 MPa, respectively; then, deionized water (without dissolved CO_2) was injected into the carbonate fracture at a flow rate of approximately 11.5 ml/h. When the downstream pressure increased to 8.00 MPa and the inlet pressure, outlet pressure, and outlet water flow rate were stable for 2 h, the upstream and downstream valves (VII and VIII) of the core holder, the water outlet valve (III and V) of the liquid container, and the water inlet valve (IX and X) of the liquid container were closed in turn. The gas container outlet valve (I) and the gas inlet valve (II and IV) of the liquid container were opened. Supercritical CO_2 was injected into the liquid container from the gas container for 12 h. Then, the water of the liquid container was sampled for pH testing to ensure that the deionized water was completely saturated with CO_2 . The injection pressure (8.00 MPa) was controlled by the degree of opening of the gas container outlet valve (I). When deionized water was saturated with CO_2 , the sample was kept at an initial pressure of 8.00 MPa and the temperature for the water and rock core remained at the experimental temperature. After the process, the gas container outlet valve (I) and the gas inlet valve (II and IV) of the liquid container were closed. The water inlet valve (IX and X) of the liquid container, the water outlet valve (III and V) of the liquid container, and the upstream and downstream valves (VII and VIII) of the core holder were opened in turn. The CO_2 -saturated water was injected into the carbonate fracture at a flow rate of approximately 11.5 ml/h. The pressures at the core inlet and outlet were recorded during the experiment. The volumetric flow rate of the outlet water was recorded using the electronic scale in the measuring system. The outlet water was sampled at intervals of 8 h for ion analysis. The output solution was collected in 10 ml centrifuge tubes that contained 1 μl of concentrated nitric acid. The acid was used to prevent any carbonate precipitation due to depressurization and degassing during sampling. Chemical analysis of the samples was carried out by using inductive coupled plasma-atomic emission spectroscopy (ICP-AES).

The experimental procedures for the four samples were identical. The temperature of the basin ranges from 30 to 60°C for the Keluke formation [21]. The experimental temperatures for S_1 , S_2 , S_3 , and S_4 were 60, 50, 40, and 60°C,

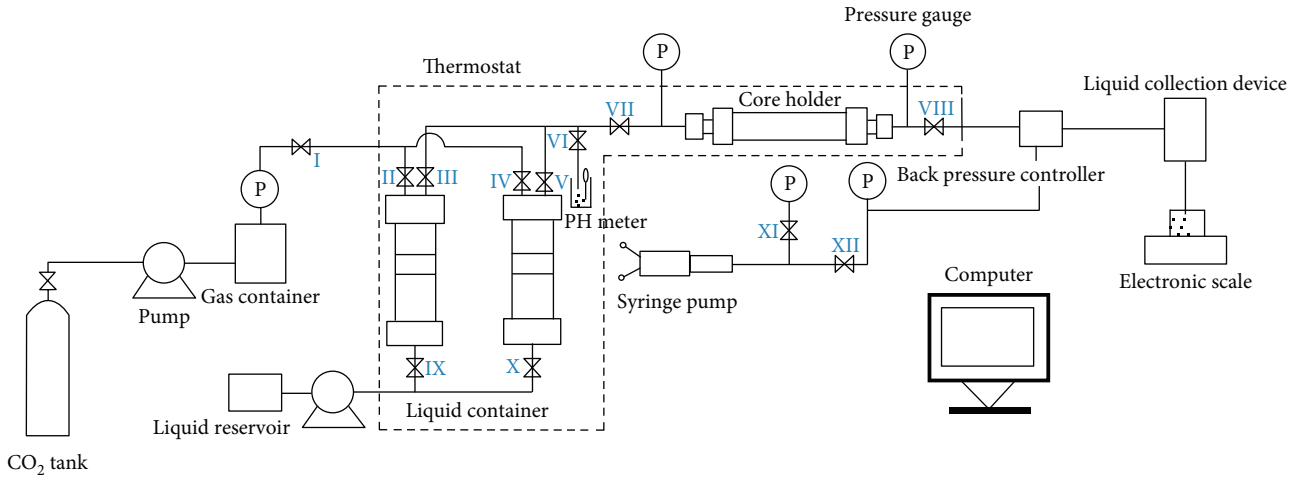


FIGURE 2: Schematic diagram of the experimental apparatus.

respectively. The experiments for S_1 , S_2 , S_3 , and S_4 lasted 96, 208, 216, and 216 h, respectively.

2.4. Solubility of Calcite under Experimental Conditions. The solubility of calcite is one of the important factors affecting the rate of carbonate dissolution [33, 34]. We performed experiments to determine the solubility for the four carbonate samples under the conditions corresponding to the CFDE experiments.

The fresh bulk corresponding experimental carbonate samples were crushed, ground, and then sieved to obtain the size fraction between $1500\ \mu\text{m}$ and $2000\ \mu\text{m}$. Ultrafine particles produced by grinding were removed by ultrasonic cleaning in alcohol. Each experiment was performed by placing the crushed material ($\sim 2\ \text{g}$) into a 500 ml reactor filled with 450 ml of pure water. The reactor was sealed; then, supercritical CO_2 was injected into the reactor for 12 h at a constant pressure (8.00 MPa) by the pump from the CO_2 tank to ensure that the deionized water was completely saturated with CO_2 . At the same time, when water was saturated with CO_2 , the temperature was set to 60, 50, 40, and 60°C for S_1 , S_2 , S_3 , and S_4 , respectively. Three hours later, the temperature was stable. Sampling of reacted solutions was performed regularly at 8 h intervals for the initial three days, after which the sample frequency was reduced to two samples per day for the fourth and fifth days and then further reduced to one sample per day for the last few days. The sample solutions were filtered by using syringes equipped with $0.45\ \mu\text{m}$ filters. The ion concentration of the sample solutions was determined by inductive coupled plasma-atomic emission spectroscopy (ICP-AES). A schematic diagram of the solubility measurement apparatus is presented in Figure 3. Figure 4 shows the results of the variations in the Ca^{2+} concentration over time.

3. Experimental Results and Discussion

3.1. Phenomenon of Channelizing Dissolution. Figure 5 shows the photographs and scanning images of the fracture surfaces before and after the CFDE experiments. In Figure 5, column

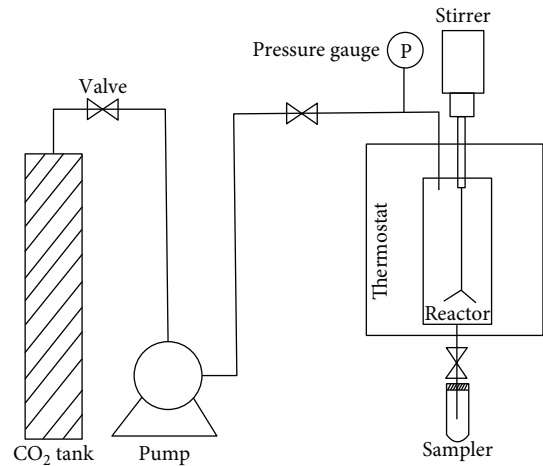


FIGURE 3: Schematic diagram of the calcite solubility measurement apparatus.

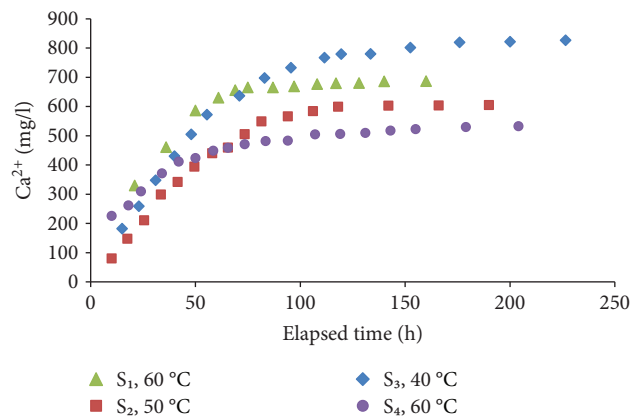


FIGURE 4: Variation in the Ca^{2+} concentration over time in the solubility measurement experiments.

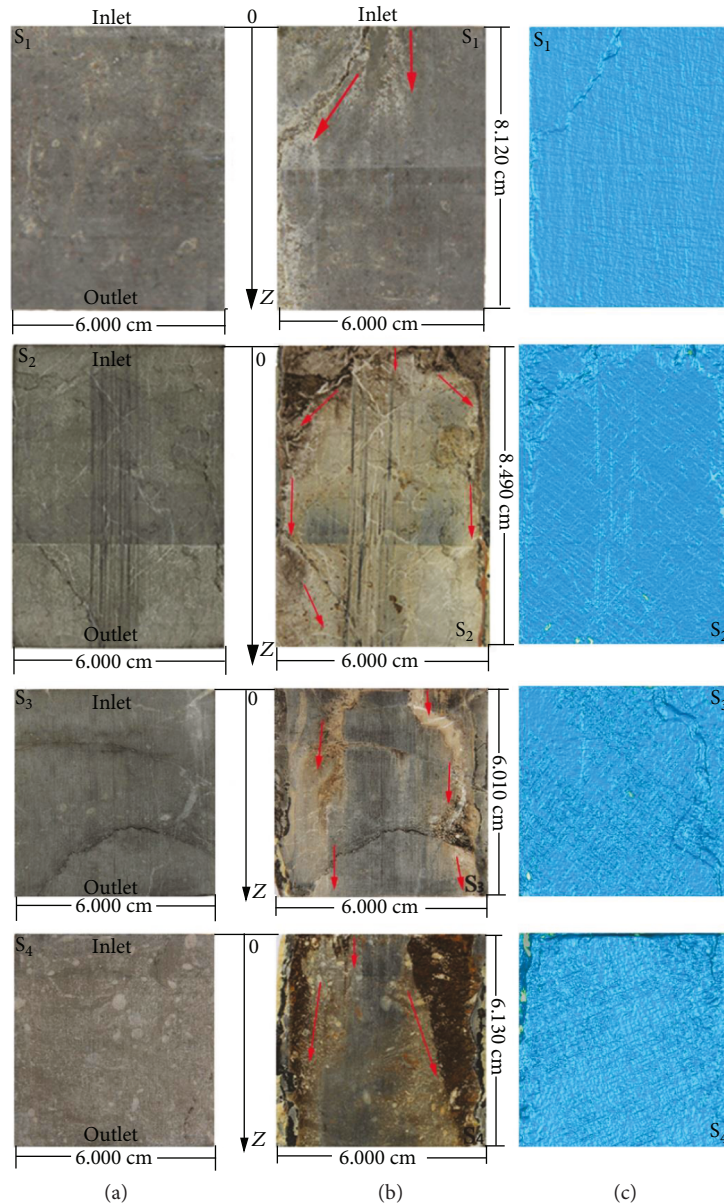


FIGURE 5: Photographs of the four fracture surfaces. Column (a) shows the photographs before the CFDE experiments. Column (b) shows the photographs after the CFDE experiments. Column (c) shows the figures of 3D-laser scanning after the CFDE experiments. The red arrow indicates the direction of flow paths and dissolution channels.

(a) shows the photographs before the CFDE experiments, column (b) shows the photographs after the CFDE experiments, and column (c) shows the images of 3D-laser scanning after the CFDE experiments.

The development of a single channel can be clearly observed in the case of S_1 . The channel started at the center of the inlet side and extended to the left side of the surface. At the inlet side, the channel width and depth are approximately 2 mm and 0.6 mm. Overall, the dissolution channel becomes gradually narrower and shallower from the inlet to the outlet. Bioclastic particles and a small amount of clay minerals can be observed on the channel wall.

The image for S_2 shows dissolution throughout the majority of the fracture surface. From the inlet ($z = 0$) to $z = 5$ mm,

uniform dissolution occurs and the dissolution depth is approximately 0.9 mm. Thereafter, the passage becomes two channels along both sides (left and right sides) of the surface; the channels are wider at $z = 5$ mm and narrow down toward $z = 52.5$ mm (the width of the left channel is 1.5 mm, and the width of the right channel is 0.1 mm). Then, from $z = 52.5$ mm, the channels on both sides widen and became shallow again. Overall, the dissolution channels are gradually shallow from the inlet to the outlet (average depth from $500 \mu\text{m}$ to $80 \mu\text{m}$). In the area around the inlet, the dissolution occurs evenly on the whole surface of the fracture. From the position of $z = 5$ mm (Figure 5), two dissolution passages form. The channels are likely along microfractures. Therefore, we suggest that

microfractures in rocks may contribute to the dissolution of carbonate rocks.

For S_3 , two channels extend from the inlet side to the outlet side. One of them develops along veins and stylolite. This suggests that veins and stylolite are likely to be preferential passages in rocks for dissolution enlargement. The right-side half is completely channelized. From the inlet to approximately $z = 7$ mm, the right channel is gradually displaced to the edge of the right side of the core surface. This displacement phenomenon is attributed to the calcite vein of the core surface. However, at approximately $z = 35$ mm, the right channel extends from the edge of the right side of the core surface to the center of the fracture surface, likely because of the mineral heterogeneity. The width and depth of the right channel at the inlet are approximately 3.8 mm and 1.2 mm, respectively, compared to 1.5 mm and 1.0 mm, respectively, at the outlet. The width and depth of the left channel at the inlet are approximately 4.0 mm and 0.7 mm, respectively, and the left channel extend forward by 40 mm.

For S_4 , dissolution occurred within a greater area than for S_1 and S_3 . As a result, the dissolution channels are considerably wider and shallower than those for S_1 and S_3 . The width and depth of the right channel are approximately 18 mm and 0.5 mm, respectively, and those of the left channel are approximately 16 mm and 1.0 mm, respectively. We observed one significant feature for S_4 ; at the end of the dissolution experiment, the dissolution channels were reddish brown and the edge of channels were yellow brown on the fracture surface center, suggesting that the dissolution channel extended forward of the surface center. Comparing S_1 and S_4 , a small amount of clay minerals was left on the S_1 channel wall, although the area of the S_4 channels was largely covered with a certain amount of insoluble mineral. Thus, the coating on the channel surface of S_4 is vuggy and rugged.

The CFDE experiments produced distinct dissolution. The dissolution channels developed across the four carbonate fractured samples. At the inlet, rocks were in direct contact with highly acidic water, leading to the dissolution of calcite and calcium release as well as large dissolution channels. Along the flow path, the pH increased and the water progressively became less reactive, which led to the dissolution channels gradually becoming narrower and shallower. The spatial variation in the channel along the flow direction can be attributed to the initial fracture characteristic, solute (Ca^{2+}) saturation, and mineralogical microstructure [35–37].

3.2. Changes in Fracture Aperture. When water flows through fractures, it dissolves the solid materials of the fracture walls. The fractures are enlarged, and the permeability of the fractures is enhanced. The change in fracture permeability over time was calculated from the pressure difference ΔP measured between the inlet and outlet of the carbonate fractures samples and combining Darcy's law (1) with a cubic law for flow through two parallel plates (2) [38, 39].

$$k = \frac{\mu L Q}{A \Delta P}, \quad (1)$$

$$Q = \frac{\Delta P d B_h^3}{12 \mu L}, \quad (2)$$

where k is the permeability of the carbonate fracture, μ is the dynamic viscosity of the solution (Pa·s), L is the length of the carbonate fracture samples in the flow direction (m), Q is the volumetric flow rate (m^3/s), A is the cross-sectional area perpendicular to the flow direction, ΔP is the measured pressure difference (Pa), B_h is the hydraulic aperture of the fracture (m), and d is the diameter of the core sample (m).

Combining (1) with (2), the hydraulic aperture of the fracture was determined by

$$B_h = \sqrt[3]{\frac{12 \mu L Q}{\Delta P d}}. \quad (3)$$

The fracture permeability is

$$k = \frac{B_h^2}{12}. \quad (4)$$

Figure 6 shows the variation process of the outflow rates in the experiments. For the four CFDE experiments, the outflow rates decrease slightly over time according to the trend line equation.

The water pressures at the inlet and outlet were measured throughout the experiment. Figure 7 shows the variation in ΔP over time during the CFDE experiments. At the beginning of the experiments, ΔP gradually decreased with time and then gradually became stable.

Figure 8 shows the variation in B_h for the four CFDE experiments. When the CO_2 -saturated water passes through the fractures, it dissolves the carbonate of the walls. The dissolved carbonate is taken away by the water such that B_h generally becomes larger. As shown in Figure 8, the hydraulic apertures of S_1 , S_3 , and S_4 are notably increased. B_h of S_2 decreases slightly in the first 168 h and then begins to increase gradually.

A slight decrease in the aperture of S_2 in the early stage of the experiment may be attributed to the initial fracture surface characteristic. Similar to some natural fractures, the surface of S_2 is uneven and jagged. At the beginning of the CFDE experiment, S_2 holds the largest hydraulic aperture in the four fractures. With the progression of the dissolution of the fracture walls, the fracture surfaces gradually become flat, and the fracture is closed under the effect of the same confining pressure.

The B_h growth rate of S_1 was the largest. Overall, the B_h values of the four fractures were enlarged by 3.4, 0.94, 1.4, and 1.2 times by the CFDE experiments, respectively.

According to Figure 8, the hydraulic aperture was a function of time. B_h can be calculated as

$$B_{h1} = \frac{4.6 + \ln(1 + 0.02351t)}{1 + e^{5.9521 - 0.1685t}} + 2.553, \quad (5)$$

$$B_{h2} = 0.000025(t - 160)^2 + 8.9688, \quad (6)$$

$$B_{h3} = 0.69 \ln(1 + 0.253t) + 6.85839, \quad (7)$$

$$B_{h4} = 0.235 \ln(1 + 4.73t) + 6.7505. \quad (8)$$

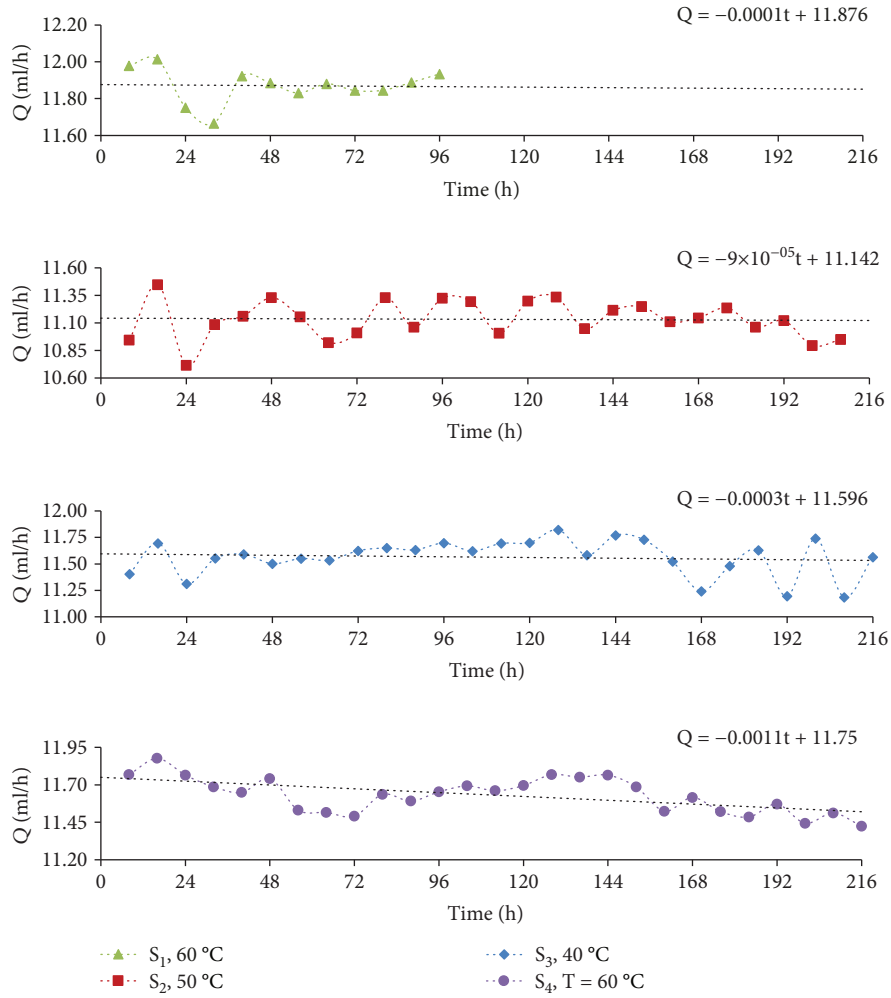


FIGURE 6: Variation process of the outflow rates.

In the above equations, B_{h1} , B_{h2} , B_{h3} , and B_{h4} are the hydraulic apertures of S_1 , S_2 , S_3 , and S_4 , respectively (μm), and t is the experimental time (h).

These formulas ((5), (6), (7), and (8)) can be divided into three categories: S type, logarithmic type, and polynomial type. The growth rate of B_{h1} can be divided into three stages: the slow growth stage, rapid growth stage, and slow growth stage. In the first slow growth stage, the flow field was uniform. However, preferential flow gradually formed with the selective dissolution of the fractured surface. Once the preferential flow path in the flow field on the fractured surface was established, the aperture growth rate entered a stage of rapid development. During the rapid growth stage, the channels formed and widened, finally reaching the steady state. In the steady state of the channel, the aperture growth rate entered a stage of slow development again.

Because the fracture surface characteristics are different, the duration of the first stage is also different. A more uneven surface is associated with a bigger initial aperture (B_0) and shorter time to establish the priority flow. Therefore, S_3 and S_4 have no clear first stage, and S_3 and S_4 belong to the logarithmic type. For S_3 and S_4 , preferential flow forms rapidly,

and then channels begin to develop. The coefficients of the formula and curve characteristics for S_3 and S_4 differ due to the experimental temperature and the mineral composition of the fracture surface.

The duration of the rapid growth stage of S_4 was shorter than that of S_3 . According to Section 3.3, because the experimental temperature of S_4 was high, the dissolution rate was fast. The growth rate of B_h is also large. However, S_4 contains a large amount of insoluble minerals. With the dissolution of the fractured surface, the coating of insoluble minerals hinders the flow and dissolution. Therefore, at the third stage, the growth rate of B_h is very slow and gradually decreases.

For S_3 , its experimental temperature was low, but the calcite content in the rock was extremely high. Although its dissolution rate was low, the rock sample was nearly completely dissolved. The dissolution channel gradually widened and deepened. The water flow rate in the channel gradually accelerated. Thus, the growth rate of B_h decreases continuously.

S_2 belongs to the polynomial type. However, B_h became larger at the end of the experiment. The latter changes of S_2 may also become a logarithmic type.

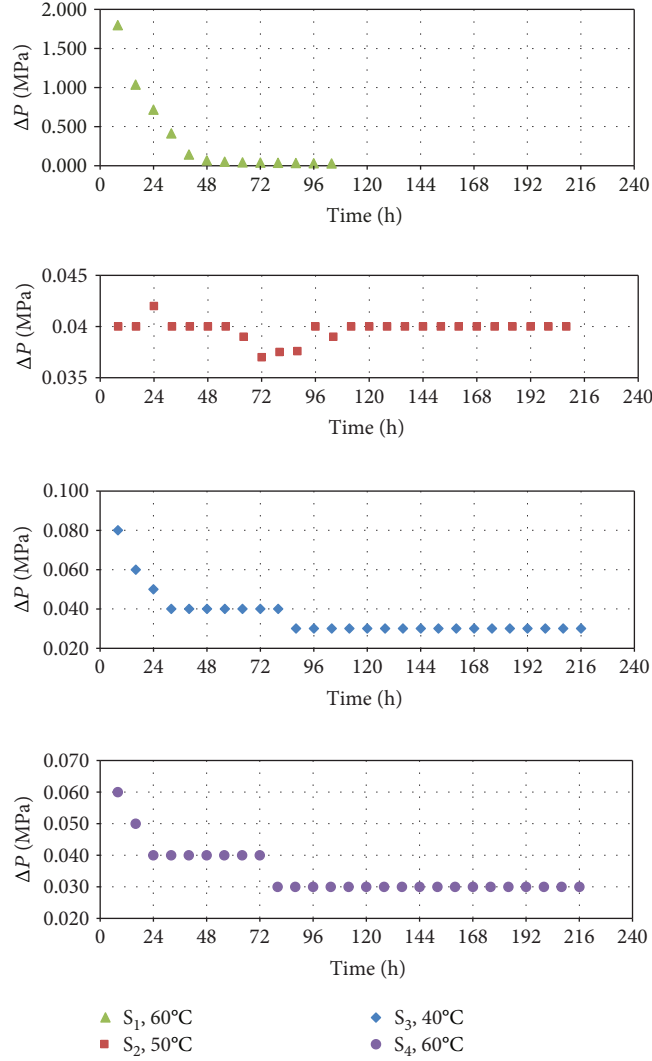


FIGURE 7: Variation process of the pressure difference.

Based on the CaCO_3 stoichiometric ratio, the total number of moles of dissolved calcite was calculated as

$$n = \frac{\sum_{i=1}^m C_i Q_i \Delta t}{M_{\text{Ca}}}, \quad (9)$$

where n is the total number of moles of dissolved calcite, M_{Ca} is the molar mass of calcium (g/mol), C_i is the Ca^{2+} concentration of the i th sample at outlet (mg/l), Q is the outflow rate of the i th sampling (m^3/s), Δt is the sampling time interval (s), and m is the total number of sampling times.

The mass of dissolved rock was calculated as

$$m_{\text{cal}} = \frac{nM_{\text{cal}}}{\alpha}, \quad (10)$$

where m_{cal} is the mass of dissolved calcite (g), α is the weight fraction of calcite in the rock samples, and M_{cal} is the molar mass of calcite (g/mol).

The volume of dissolved rock was calculated as

$$V_{\text{cal}} = \frac{m_{\text{cal}}}{\rho_{\text{cal}}}, \quad (11)$$

where V_{cal} is the volume of dissolved rock (m^3) and ρ_{cal} is the rock density (kg/m^3), and the value of ρ_{cal} was $2800 \text{ kg}/\text{m}^3$.

The dissolution aperture was calculated as

$$B_d = \frac{V_{\text{cal}}}{A_{\text{lw}}} = \frac{V_{\text{cal}}}{Ld}, \quad (12)$$

where B_d is the dissolution aperture and A_{lw} is the reaction area (m^2). Namely, A_{lw} is the sample diameter times the sample length.

Figure 9 shows the increasing trends for the dissolution aperture of the four fractures. In Figure 9, B_d increased nearly linearly over time, indicating that B_d increases at a constant rate. According to the slope of B_d , the growth rate of B_d was the largest for S_2 and the smallest for S_1 . These results can be attributed to the experimental temperatures and reaction area.

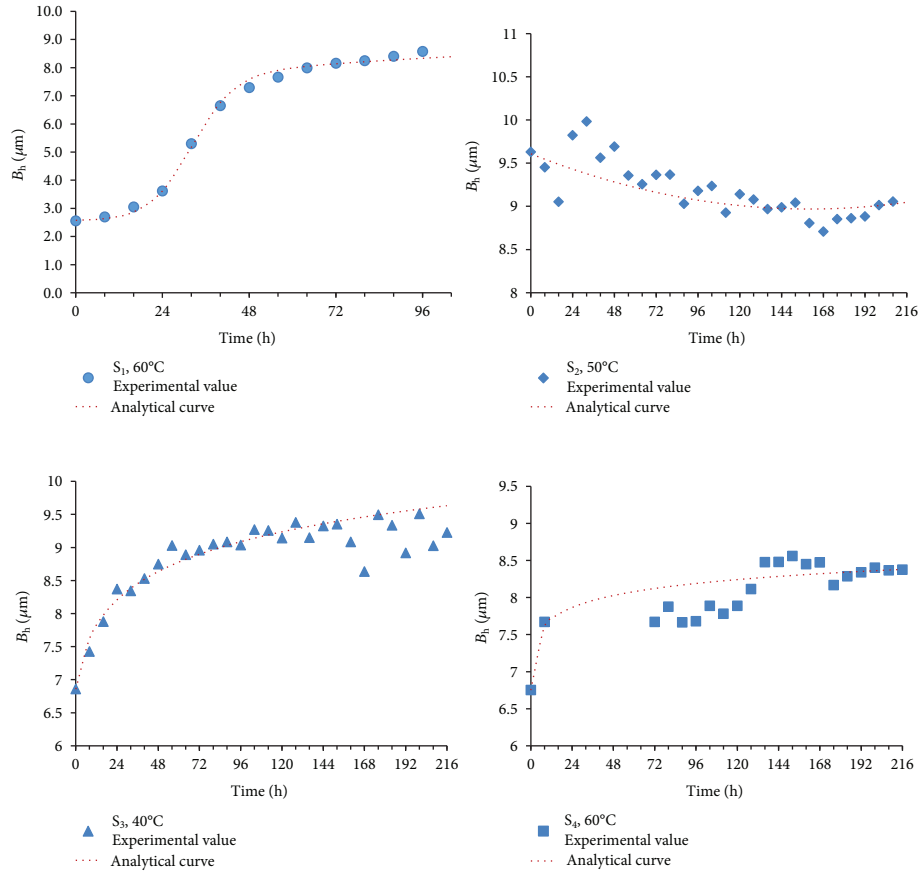


FIGURE 8: Hydraulic apertures of the fractures over time during the CFDE experiments.

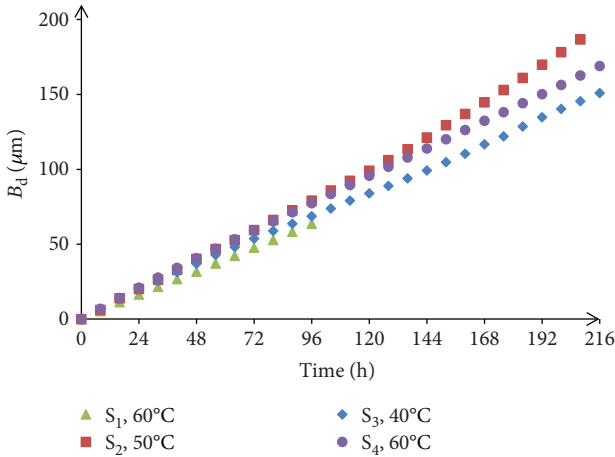


FIGURE 9: Dissolution apertures of the fractures over time during the CFDE experiments.

A comparison of Figures 8 and 9 indicates that the values of B_d were approximately one order of magnitude larger than those of B_h . This result can be attributed to the fracture dissolution characteristic along the flow direction. The dissolution channels gradually became narrower and shallower from the inlet to the outlet. Namely, the actual aperture of the samples gradually decreased along the flow direction. According to the groundwater dynamics calculation, the

permeability of a heterogeneous fracture was mainly controlled by the narrow parts. Dissolution enlargement in the area around the outlet was slow for all four fractures, resulting in the slow increases in the permeability and B_h of the fractures.

B_d was defined as the average dissolution aperture openness. The carbonate dissolution was mainly located at the inlet end, and the dissolution aperture was larger than B_h . Therefore, B_d was larger than B_h .

3.3. Ca^{2+} Concentration at the Outlet and Dissolution Rate

3.3.1. Solubility Results of the Samples. Figure 4 shows that the Ca^{2+} concentrations increased during the experiments, and the release rates (the slopes of the curves in Figure 4) decreased over time as the reacted aqueous solutions approached saturation with respect to calcite. The slopes given by the last three points tend to zero, indicating that the dissolution reaction has approached equilibrium. We use the average of the last three numbers for the calcium equilibrium concentration. The calcite solubility results and the experimental conditions are shown in Table 3.

The temperature plays a significant role in solubility, and the original textures and structure of the samples as well as the mineralogical and chemical composition also affect the solubility. Generally, for S_2 , S_3 , and S_4 , the calcite solubility increases with decreasing of temperature. The solubility of

TABLE 3: The calcite solubility of the carbonate samples under the CFDE experimental conditions.

Sample	Temperature (°C)	Pressure (MPa)	Ca ²⁺ (mg/L)
S ₁	60	8	684.341
S ₂	50	8	603.780
S ₃	40	8	822.667
S ₄	60	8	528.500

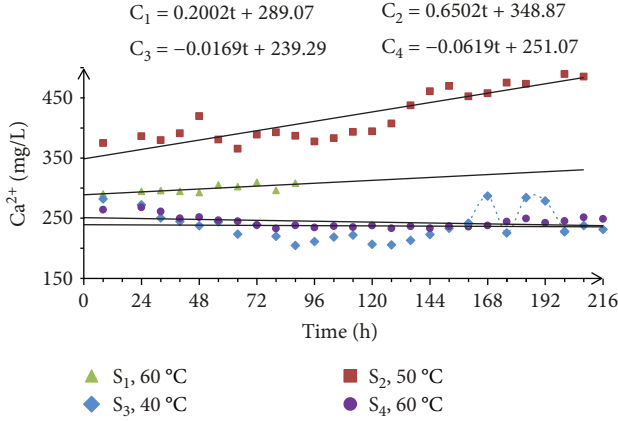
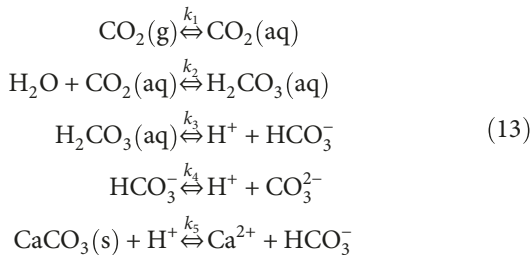


FIGURE 10: Variation in the Ca²⁺ concentration over time. The dotted line data refers to the ICP instrument being rebooted due to the replacement of the instrument operation gas.

calcite increases with increasing calcium oxide content in the carbonate samples (S₁). Therefore, the experimental solubility for the four samples is different.

3.3.2. Dissolution Rate of Fractured Carbonate. Figure 10 illustrates the variation in the Ca²⁺ concentration over time during the experiments. Overall, the Ca²⁺ concentration of S₂ was higher than those for the other samples. This result is attributed to the experimental temperature. Carbonate dissolution is mainly controlled by the reactions occurring within the ternary system water (H₂O), carbon dioxide (CO₂), and calcite (CaCO₃) [40–44]. The chemical reactions and process responsible for the removal of calcite are



The first reaction describes the physical dissolution of CO₂ in water. The second reaction describes the conversion of CO₂ into carbonic acid. The third and fourth reactions are the primary ionization and secondary ionization of carbonic acid, respectively. Namely, the third reaction is the conversion of carbonic acid into hydrogen and bicarbonate, and the fourth reaction is the dissociation of bicarbonate into

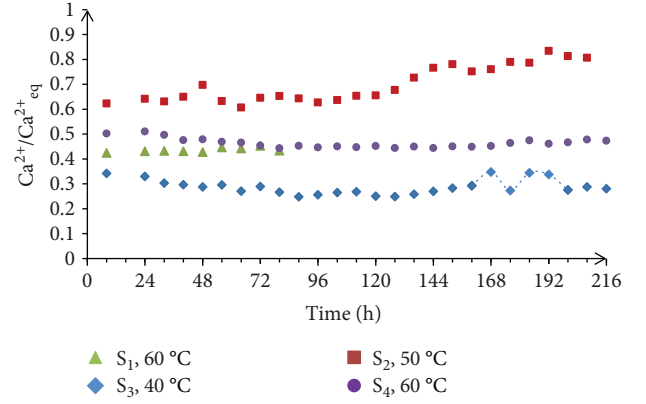


FIGURE 11: Variation in Ca²⁺/Ca²⁺_{eq} over time. The dotted line data refers to the ICP instrument being rebooted due to the replacement of the instrument operation gas.

hydrogen and carbonate ions. The fifth reaction is the dissolution of calcite. This dissolution reaction was affected by the H⁺ concentration at the solid-liquid interface. The hydrogen ions in the solution are produced by the ionization of carbonic acid. Because the secondary ionization constant of carbonic acid is four orders of magnitude lower than the primary ionization constant, the secondary ionization of carbonic acid can be neglected.

Figure 11 illustrates the variation in Ca²⁺/Ca²⁺_{eq} versus time. Figure 11 shows that the dissolution reactions of the four samples are far from the equilibrium reaction. Therefore, the fifth reaction is in the positive reaction direction. In this paper, the partial pressure of CO₂ is the same for all the samples, and the amount of CO₂ is sufficiently excessive. Therefore, the H⁺ concentration was controlled by the primary ionization constant. According to Plummer and Busenberg [45], k_3 is a function of temperature and can be calculated as

$$\begin{aligned}
 \log k_3 = &-356.3094 - 0.06091964T + \frac{21834.37}{T} \\
 &+ 126.8339 \log T - \frac{1684915}{T^2},
 \end{aligned} \quad (14)$$

where k_3 is the primary ionization constant of carbonic acid and T is the absolute temperature.

According to (14) and Figure 12, k_3 was the largest at 50°C and the smallest at 40°C. Namely, the conversion rate of carbonic acid into hydrogen was the largest at 50°C and the smallest at 40°C. The H⁺ concentration was the largest at 50°C and the smallest at 40°C [46]. The Ca²⁺ concentration was the highest at 50°C and the smallest at 40°C.

However, the Ca²⁺ concentration of S₄ was lower than that of S₃ at a given time, which can be attributed to the mineral composition of S₄. With the dissolution, the fracture surface of S₄ was covered with a layer of refractory minerals. The refractory minerals might lead to a reduction in calcite dissolution. Overall, the Ca²⁺ concentration of S₄ was still higher than that of S₃.

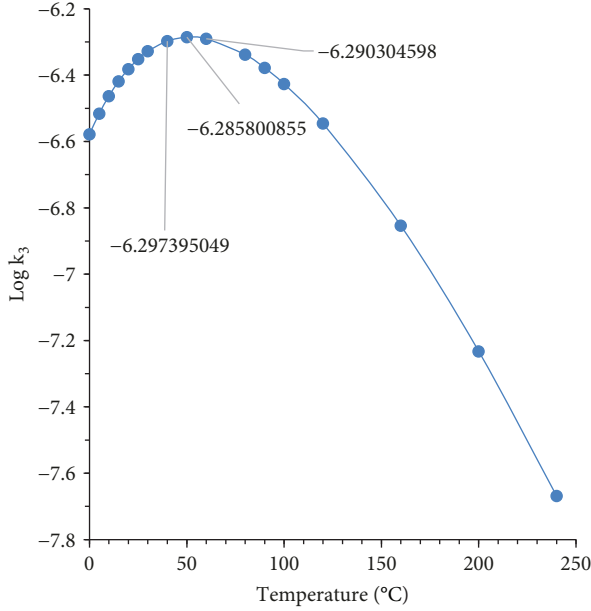


FIGURE 12: Change in the primary ionization constant of carbonic acid ($\log k_3$) with the temperature. ([45]).

For the CFDE experiments, dissolution rates of carbonate samples were related to the Ca^{2+} concentration at the solid-liquid interface and the contact area (the reaction area) of the solid-liquid surface. The contact area of a rough surface is difficult to determine and changes with the dissolution process. In the early stage, the fracture may be visualized as an opening between two parallel plates. The reaction area may be approximated with the area of the fracture surface, which is equal to the product of the length and the diameter of the core sample (A_{lw}). If the reaction area is assumed to be constant within the first 96 h, the dissolved volume of carbonate rock within the first 96 h can be determined by combining (9), (10), and (11).

The dissolution rates of carbonate samples were calculated as

$$F_{lw} = \frac{V_{lw}}{2v_{cal}A_{lw}t}, \quad (15)$$

where V_{lw} is the dissolved volume of carbonate rock within 96 h (m^3), v_{cal} is the molar volume of carbonate rock ($3.69 \times 10^{-5} \text{ m}^3/\text{mol}$), A_{lw} is half of the reaction area (m^2) because of the fracture having two surfaces, and t is the reaction time (96 h).

The dissolution rates (F_{lw}) were calculated using (15) and are shown in Table 4. According to Table 4, the values of the dissolution rate are about one order of magnitude greater than that provided by Kirstein et al. [20]. Meanwhile, the dissolution rates in this paper are approximately equal to that of Cao et al. [2]. Also, the dissolution rate is four times smaller than that of Elkhoury et al. [26]. The differences in dissolution rates among the authors can be attributed to the experimental temperature, pressure, flow rate, and other factors.

Additionally, the dissolution rate of carbonate rock was the largest at 50°C. Kaufmann and Dreybrodt [10] stated that the carbonate dissolution rate is determined by the Ca^{2+} concentration at this fracture, by the conversion rate of carbonic acid into H^+ in the solution, and by diffusional mass transport of the dissolved species from and toward the water-rock interface. According to (14), the conversion rate of carbonic acid into hydrogen was largest at 50°C. You et al. [47] studied the aqueous solution of calcium carbonate via molecular dynamics simulation and found that the diffusion coefficient of water molecules increases with increases in temperature and is relatively small only when the temperature is 333 K. From 40 to 60°C, the diffusion coefficient of water molecules was the largest at 50°C. Therefore, at 50°C, the highest dissolution rate of carbonate rock was attributed to the largest conversion rate of carbonic acid into H^+ and the largest diffusion coefficient of water molecules.

3.4. Dissolution Patterns. The dissolution mechanic of the fracture surfaces can be separated into three steps: (i) ions dissociate from the surface due to thermodynamic disequilibrium at the mineral surface; (ii) ions diffuse away from the surface due to the concentration gradient created by the dissolution reaction; and (iii) ions are transported through the fracture by advection. The relative rates of the reaction, diffusion, and advective transport of Ca^{2+} control the nature of the dissolution process within the fracture and the evolution of the fracture permeability and morphology [48–52]. The effective kinetic is controlled by the slowest of these three steps. If the characteristic time of the reaction is short compared to the characteristic time of transport (advection versus diffusion), the process is transport limited. Conversely, a reaction-controlled process means that compared with mass transport (either advection or diffusion), the reaction is slow and dissolution is limited by the dissolution reaction rate. The relative strength of advection, diffusion, and reaction can be accurately represented by two important dimensionless numbers, the Peclet number (P_e) and the Damkohler number (D_a) [53]. Different dissolution patterns may be observed depending on the values of these numbers: face dissolution (only dissolution at the inlet and no further alteration along the fracture due to reactant consumption), channel (preferential flow path) formation, or uniform dissolution along the core [28, 49, 50, 52, 54].

In the formulation employed here, The P_e number is given by

$$P_e = \frac{\nu B_{h0}}{D_m}, \quad (16)$$

where ν is the fluid velocity in m/s, B_{h0} is the initial hydraulic aperture of the fracture in m, and D_m is the molecular diffusion coefficient of the reactants in m^2/s .

ν is defined as

$$\nu = \frac{Q}{dB_{h0}}, \quad (17)$$

TABLE 4: The dissolution rate of the CFDE experiments.

Sample	Length (cm)	Width (cm)	Confining pressure (MPa)	Back pressure (MPa)	Temperature (°C)	Solution	P _{CO₂} (MPa)	pH	Flow rate (ml/min)	Average [Ca ²⁺] (mg/l)	Average dissolution rate (mol/m ² /s)
S ₁	8.12	6.00	20	8	60		8		0.2	303.16	2.50×10^{-6}
S ₂	8.49	6.00	20	8	50	CO ₂ -rich water	8		0.2	372.02	3.11×10^{-6}
S ₃	6.01	6.00	20	8	40		8		0.2	239.30	2.70×10^{-6}
S ₄	6.13	6.00	20	8	60		8		0.2	245.13	3.04×10^{-6}
Micritic limestone	Crushed materials				5	H ₂ SO ₄		4.7	1.8		2.42×10^{-7}
	Crushed materials				26			4.7	1.8		10.88×10^{-7}
Sparitic limestone	Crushed materials				5	H ₂ SO ₄		4.7	1.8		4.19×10^{-7}
	Crushed materials				26			4.7	1.8		7.74×10^{-7}
Cement core	22.48	3.72	6343	4137	25	CO ₂ -rich brine	68.9	3.9	0.498	250	
V1	4.71	3.81	28.9	14.3	61	CO ₂ -rich water	12.5		0.23	1360	
V2	4.88	3.81	28.8	14.3	61		12.5		0.1	1380	

Note: The data on S₁, S₂, S₃, and S₄ come from this paper. The data on micritic limestone and sparitic limestone come from Kirstein et al. [20]. The data on cement core come from Cao et al. [2]. The data on V1 and V2 come from Elkhoury et al. [26].

TABLE 5: Summary of the experimental samples and kinetic parameters (the value of D_m is from You et al., [47]).

Parameter (unit)	Description	$S_1, 60^\circ\text{C}$	$S_2, 50^\circ\text{C}$	$S_3, 40^\circ\text{C}$	$S_4, 60^\circ\text{C}$
B_{h0} (m)	Initial hydraulic aperture	2.53×10^{-6}	9.63×10^{-6}	6.86×10^{-6}	6.75×10^{-6}
v (m/s)	Average velocity	2.17×10^{-2}	5.35×10^{-3}	7.80×10^{-3}	7.98×10^{-3}
D_m (m ² /s)	Molecular diffusion coefficient	5.75×10^{-10}	3.00×10^{-10}	1.50×10^{-10}	5.75×10^{-10}
P_e	Peclet number	48	74	178	47
D_a	Damkohler number	2.97×10^{-7}	2.31×10^{-6}	3.34×10^{-6}	9.63×10^{-7}

where Q is the outflow rate in m³/s and d is the width of the fracture in m; the width is equal to the diameter of the samples in the paper.

According to Tartakovsky et al. [55] and Lichtner and Kang [56], D_a is defined as

$$D_a = \frac{K_{lw} B_{h0}}{D_m}, \quad (18)$$

where K_{lw} is the dissolution rate constant. According to Kirstein et al. [20], K_{lw} can be assumed as $K_{lw} = F_{lw}$ (m/s).

According to (16) and (18), D_a characterizes the first and second steps of the fracture surface dissolution mechanic and P_e characterizes the second and third steps of the fracture surface dissolution mechanic. The P_e and D_a values were computed and are shown in Table 5. The P_e and D_a values were always greater than one and thus denote a diffusion-controlled process for the samples. Larger P_e and D_a values are associated with a smaller relative diffusion rate of Ca²⁺ and thus a more notable channelizing dissolution.

In addition, advection is also one of the important factors that affect the solute diffusion. For the samples, a higher advective velocity is associated with a larger P_e value. The higher velocity denotes that the hydrodynamic renewal of the reactive fluid is high at the fluid-rock interface along the water flow direction. Namely, the large dissolution channels are easily formed along the water flow direction. As expected for sample S_3 , at this relatively high velocity, the fast reactant renewing in the fracture leads to the development of distinct large-scale dissolution channels (Figure 5). For sample S_2 , the reactive fluid renewing is slow along the water flow direction. The dissolution of S_2 is evenly advanced forward. Therefore, the S_2 dissolved site is mainly located at the entrance end, and its dissolution pattern belongs to the transition from face dissolution to the channel.

The D_a values for S_1 and S_4 are smaller than those for S_2 and S_3 , indicating that the diffusion rate is small but its effect is not significant, in contrast to the reaction rate. However, the advective velocity of S_1 is one order of magnitude larger than that of S_4 . As expected, S_1 was dissolved to form a distinct large-scale channel. The advective velocity for S_4 was slow, and thus, the dissolution channels were wider than for S_1 .

In summary, for a diffusion-controlled process, the dissolution channel phenomenon appears with fast flow and face dissolution occurs with slow flow in the fracture. Min et al. [37] also obtained the same results.

The effects of the reaction rate and molecular diffusion strength on the dissolution patterns are controlled by the experimental temperature. A dissolution process at low temperature has higher Peclet and Damkohler numbers, thus leading to notable channelizing dissolution. The Peclet and Damkohler numbers of the CFDE experiment are the highest S_3 , and thus, the channelizing dissolution is the most notable of the four fractures.

3.5. Effect of Mineral Heterogeneities on Preferential Dissolution

3.5.1. Initial Mineralogical Characterization of the Samples.

Table 1 shows the lithology, sampling depth, and length of the samples. The matrix of these limestone samples is mainly composed of microcrystalline calcite. The samples also contain small amounts of biogenic fragments or calcite vein. The biogenic fragments of S_1 are mainly composed of coral fossils. In S_2 , multiple sets of tectonic joints formed a grid-like structure, and the joints were filled with calcite, terrestrial mud, and terrigenous sand. S_3 contains two sets of typical joints, one of which formed a low-angle tensile fracture and the other of which was a high-angle tensile fracture. The fractures were filled with biologic shells and calcite veins. S_4 contains a large number of fossils, such as fusulinida and corals. The calcite cement found in S_4 is mainly composed of microcrystalline calcite, clay minerals, and extremely low amounts of ferromagnesian and quartz.

3.5.2. Effect of Mineral Heterogeneities on Preferential Dissolution.

The CFDE experiments and SEM images provide independent parameters to characterize the dissolution progress within the fracture from the sample scale to the microscale. For fractured samples, the dimensionless Damkohler and Peclet numbers provide a means to estimate the evolution of the dissolution patterns. However, the mineralogical heterogeneities also affect the dissolution patterns and the location of the preferential channel. It is important to investigate the potential impacts of the mineral structure and chemical composition on the location of preferential channels in the fracture.

In the case of S_1 , the dissolution channel is mainly developed in locations where the bioclots are gathered (Figure 13). The bioclots are mainly gastropods, brachiopods, and echinoderms, and the size of bioclots particles is different from each other. Micritic cement of the bioclots is mainly composed of microcrystalline calcite and few clay minerals. The bioclast and micritic cements are preferential dissolution

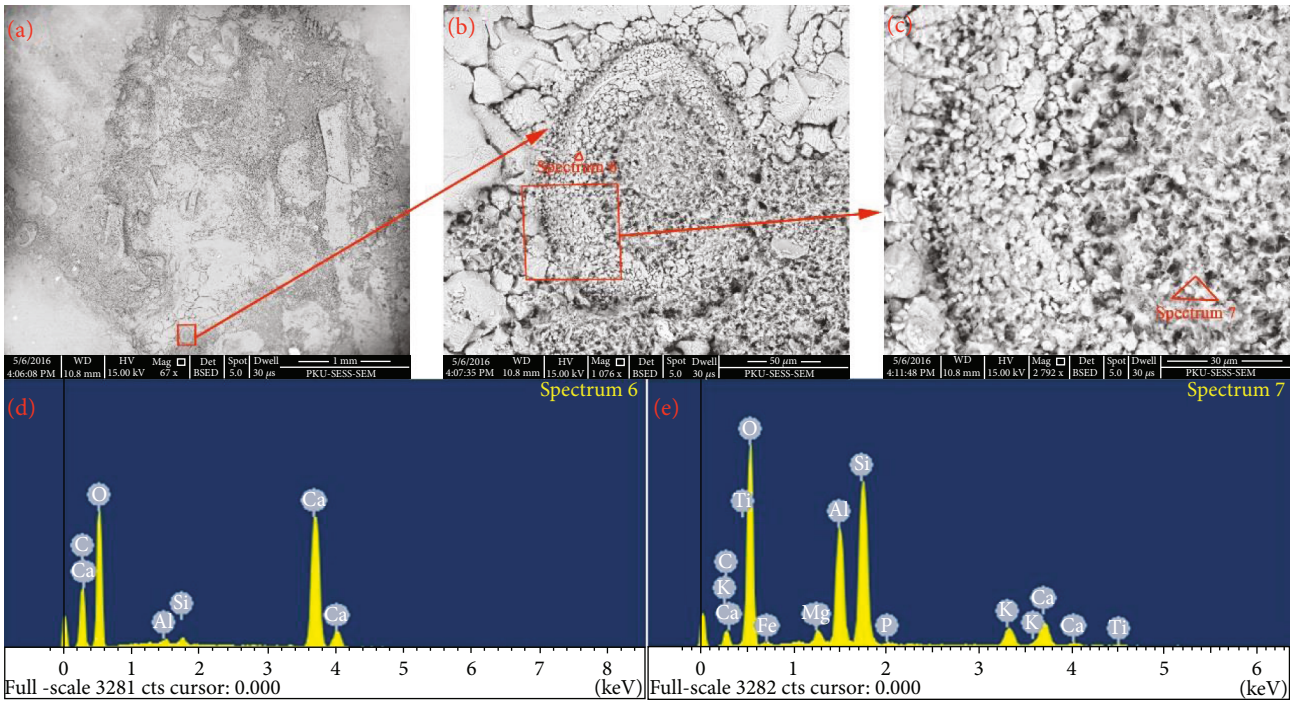


FIGURE 13: SEM photomicrographs of the bioclastic particles of S_1 . (a) Dissolved bioclastic particles. (b) Detailed view of the dissolved bioclastic particles. (c) More detailed view of the dissolved bioclastic particles. (d) EDS data of the triangle encircled part in (b). (e) EDS data of the triangle encircled part in (c).

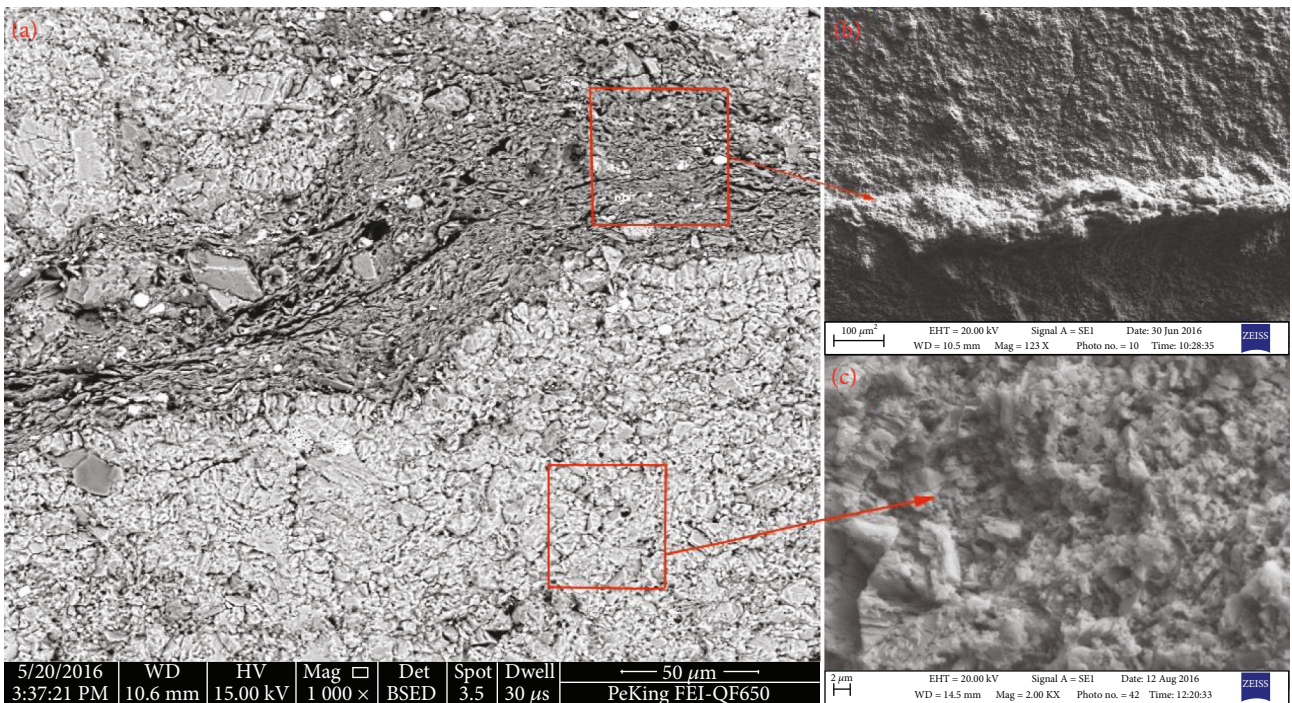


FIGURE 14: SEM photomicrographs of the calcite matrix and the later filling matter of S_2 . (a) Preexperiment SEM photomicrographs of S_2 . (b) Detailed view of the later filling matter after the CFDE experiments. (c) Detailed view of the calcite particles after the CFDE experiments.

material because they have smaller particle sizes and a looser structure. There is no doubt that the particle size is inversely proportional to the particle surface area. More tiny

interparticle pores and larger interaction area may be another reason. Saturated CO_2 aqueous solution flows along the pores between the calcite grains and biological particles,

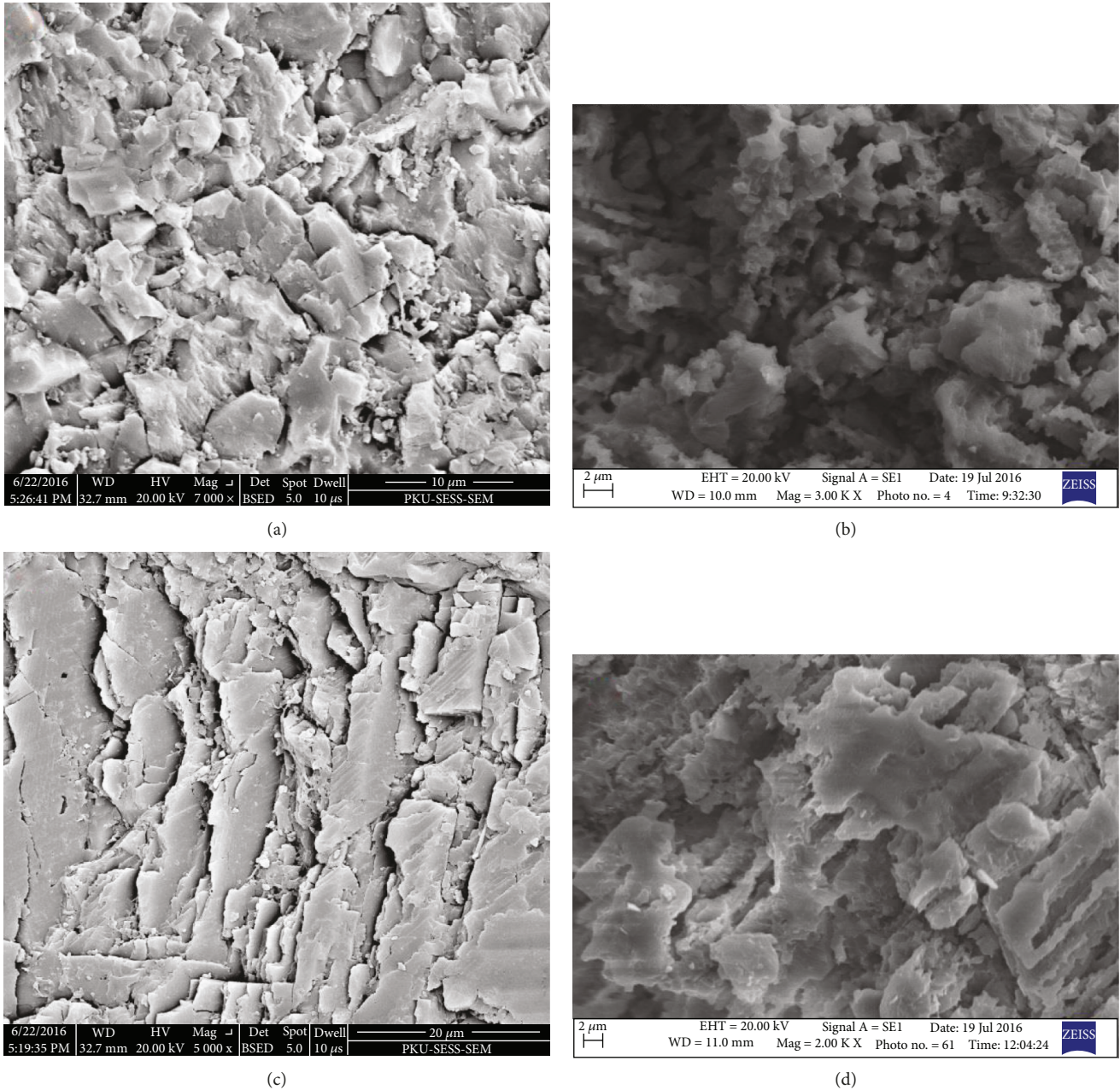


FIGURE 15: SEM photomicrographs of the calcite matrix and calcite vein of S_3 . (a) Preexperiment SEM photomicrographs of the calcite matrix. (b) Postexperiment SEM photomicrographs of the calcite matrix. (c) Preexperiment SEM photomicrographs of the calcite vein. (d) Postexperiment SEM photomicrographs of the calcite vein.

and the calcite around the pores dissolves to form enlarged interparticle dissolution pores. The microcrystalline cements of the bioclasts and microcrystalline calcite inside the bioparticles are dissolved away, and a small amount of clay minerals are left, leading to the formation of the dissolution pores and intergranular pores.

In the case of S_2 , the partially dissolved and nondissolved grains of rock were visible in the fracture surface (Figure 14). The jointing and interchange of jointing of the calcite crystal were first dissolved into micropores and microcracks, and the surface of the calcite particle was undulated and rough

(Figure 14(c)). Pores and cracks along the jointing became larger and deeper. The later filling matter was approximately parallel to the sample cross section and perpendicular to the flow direction. (Figure 14(b)) It was indissolvable and obstructed the transport of the unsaturated reaction solution. Therefore, the position of the late filling matter determines the boundary of the face dissolution. S_2 developed channels after the boundary. Therefore, the experiment for S_2 was in a transitional regime between face dissolution and channel development.

The calcite veins on the fracture surface are notable in the case of S_3 (Figure 5(a)). As shown in Figure 15, the crystal

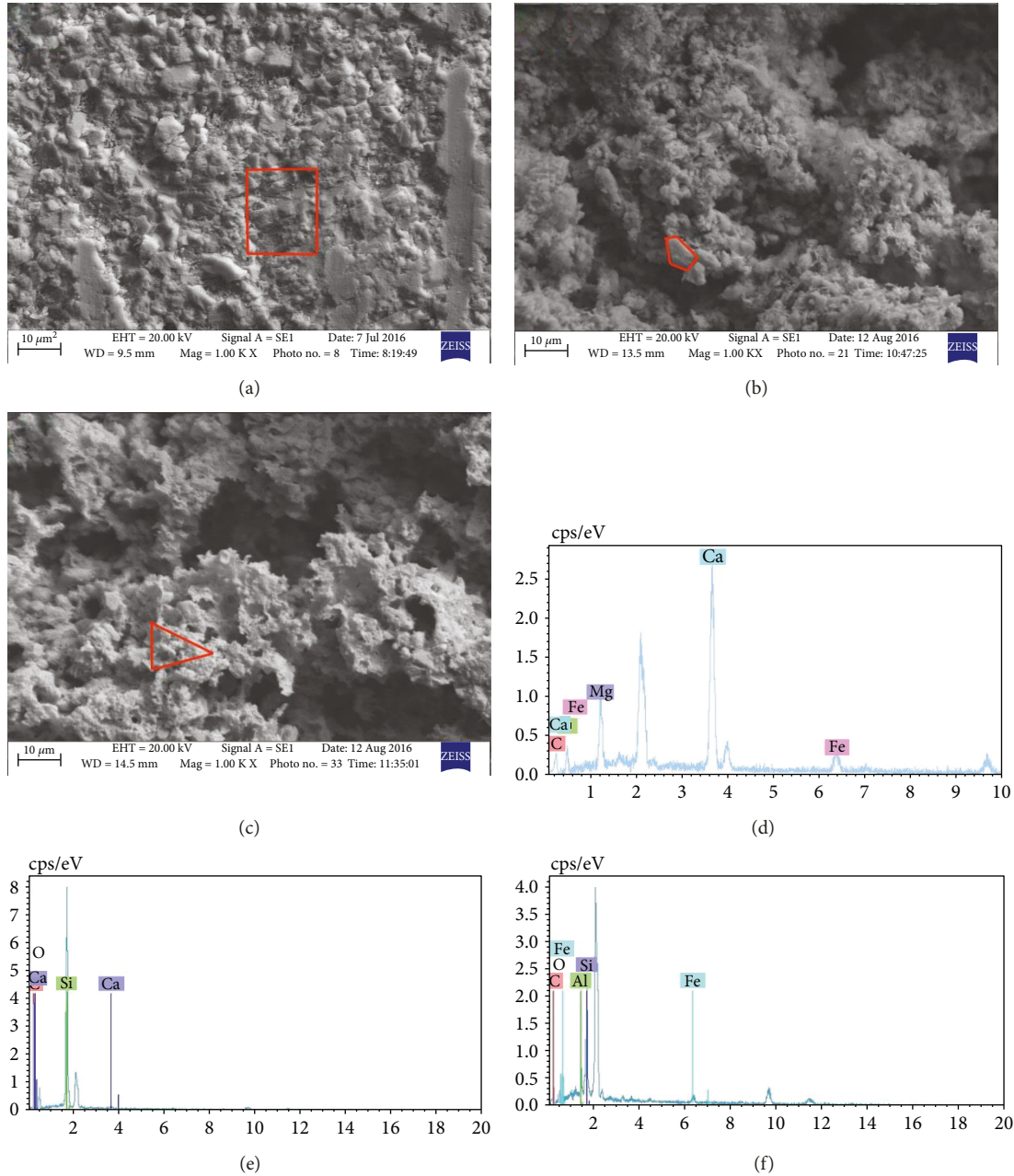


FIGURE 16: (a) Preexperiment SEM photomicrographs of the carbonate matrix of S_4 . (b) Postexperiment SEM photomicrographs of the calcite particle. (c) Postexperiment SEM photomicrographs of the nondissolved cement. (d) EDS data of the square encircled part in (a). (e) EDS data of the polygon encircled part in (b). (f) EDS data of the triangle encircled part in (c).

morphology of the calcite veins is different from that of the calcite of the carbonate matrix. Carbonate matrix calcite is irregularly granular, with a particle size of 4–10 μm (Figure 15(a)). The water along the pores of the calcite crystal grain flows such that the granular calcite is dissolved into a microcrystalline calcite and yields a large number of cracks and holes (Figure 15(b)). However, vein calcite has a clear cleavage plane, and the cleavage plane is a few to a dozen microns (Figure 15(c)). The cleavage and cleavage interchange of the vein calcite were first dissolved into micropores and microcracks. The dissolution channel locations (Figure 5(b)) of the experiment on S_3 indicate that the calcite veins

are more easily dissolved than granular calcite. Namely, calcite with cleavage is more susceptible to dissolution than granular calcite is.

In the case of S_4 (Figure 16), the crystal morphology of calcite is irregularly granular. The calcite cement is mainly composed of microcrystalline calcite, clay minerals, and extremely small amounts of ferromagnesian and quartz. In the experiment, the fracture surface mineral homogeneities caused the dominant channels to form along the flow direction. The nondissolved grains of quartz and the partially dissolved silicate grains and ankerite continued to be visible in the dissolution zone.

4. Conclusions

The photographs and 3D laser scanning images of the fracture surfaces before and after the CFDE experiments indicated that the samples developed distinct dissolution zones. The dissolution channels of S_3 and S_4 were all across the fracture surface. The dissolution channels for S_1 and S_3 were narrower, deeper, and cleaner. For S_2 , the inlet end experienced uniform dissolution and then developed into two channels. For S_4 , the channels were wide and shallow.

After the CFDE experiment, the hydraulic apertures (B_h) of sample 1 (S_1), sample 3 (S_3), and sample 4 (S_4) were enlarged by 3.4, 1.4, and 1.2 times, respectively. The aperture of sample 2 (S_2) was slightly reduced in the early stage of the experiment. B_h has three forms as a function of time: S type, logarithmic type, and polynomial type. S_1 belongs to the S type, and the S curve can be divided into three stages: the slow growth stage, rapid growth stage, and slow growth stage. S_2 belongs to the polynomial type. S_3 and S_4 belong to the logarithmic type.

The carbonate fracture dissolution rates (F_{lw}) were determined by combining the Ca^{2+} concentration and reaction area. The laboratory dissolution rate of S_1 , S_2 , S_3 , and S_4 were 2.50×10^{-6} , 3.11×10^{-6} , 2.70×10^{-6} , and 3.04×10^{-6} mol/m²/s, respectively. The dissolution rate of carbonate rock was the largest at 50°C. This result was attributed to the experimental temperature, the conversion rate of carbonic acid into H^+ , and the diffusion coefficient of water molecules.

The experiment results indicate that the dissolution pattern depends on the Peclet and Damkohler numbers for the CFDE experiments at different temperatures. A dissolution process at low temperature has a higher Peclet number, thus leading to notable channelizing dissolution. In addition, advection is one of the most important factors affecting the solute diffusion. In the large-temperature scale, at a suitable advective velocity, the dissolution patterns might change from face dissolution to a typical channel and uniform dissolution by increasing the temperature.

The SEM images and EDS data indicated that the four fracture surfaces exhibited different microstructures. The initial surface mineral heterogeneity and texture strongly affect the dissolution rate and the location of preferential dissolution in the CFDE experiments. A preferential channel typically develops in places where bioclasts are accumulated, or the calcite veins and original fractures are distributed.

Data Availability

The data used to support the findings of this study are available from the corresponding author upon request.

Conflicts of Interest

The authors declare that they have no conflicts of interest.

Acknowledgments

This work was supported and funded by the China Geological Survey and funded in part by the National Natural

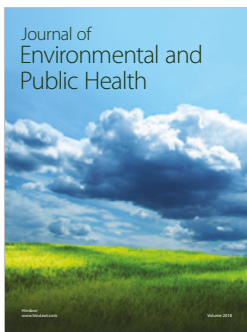
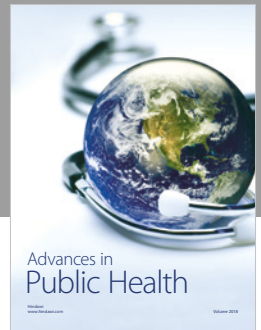
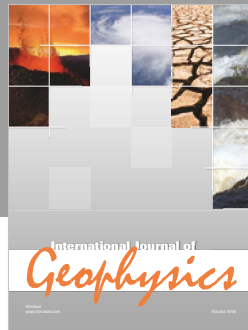
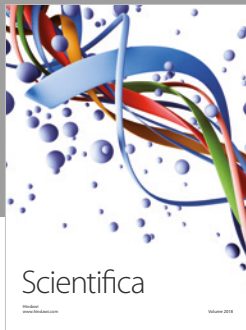
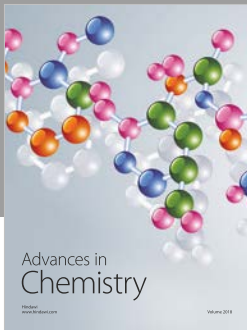
Science Foundation of China (Grant nos. U1612441, 1212011120964-03, 41272387, and 41272159). The authors would also like to thank the Institute of Geology of the Chinese Academy of Sciences for providing the 3D laser scanner and microstructure analytical laboratory at Beijing University.

References

- [1] J. I. Baceta, V. P. Wright, S. J. Beavington-Penney, and V. Pujalte, "Palaeohydrogeological control of palaeokarst macro-porosity genesis during a major sea-level lowstand: Danian of the Urbasa-Andia plateau, Navarra, North Spain," *Sedimentary Geology*, vol. 199, no. 3-4, pp. 141-169, 2007.
- [2] J. Cao, W. Hu, X. Wang et al., "Diagenesis and elemental geochemistry under varying reservoir oil saturation in the Junggar Basin of NW China: implication for differentiating hydrocarbon-bearing horizons," *Geofluids*, vol. 15, no. 3, 420 pages, 2015.
- [3] J. Feng, J. Cao, K. Hu et al., "Dissolution and its impacts on reservoir formation in moderately to deeply buried strata of mixed siliciclastic-carbonate sediments, northwestern Qaidam Basin, northwest China," *Marine and Petroleum Geology*, vol. 39, no. 1, pp. 124-137, 2013.
- [4] M. Filipponi, P. Y. Jeannin, and L. Tacher, "Evidence of inception horizons in karst conduit networks," *Geomorphology*, vol. 106, no. 1-2, pp. 86-99, 2009.
- [5] Z. Jin, D. Zhu, W. Hu, X. Zhang, J. Zhang, and Y. Song, "Mesogenetic dissolution of the middle Ordovician limestone in the Tahe oilfield of Tarim basin, NW China," *Marine and Petroleum Geology*, vol. 26, no. 6, pp. 753-763, 2009.
- [6] J. Li, W. Zhang, X. Luo, and G. Hu, "Paleokarst reservoirs and gas accumulation in the Jingbian field, Ordos Basin," *Marine and Petroleum Geology*, vol. 25, no. 4-5, pp. 401-415, 2008.
- [7] R. G. Loucks, "Paleocave carbonate reservoirs: origins, burial-depth modifications, spatial complexity, and reservoir implications," *AAPG Bulletin*, vol. 83, no. 11, pp. 1795-1834, 1999.
- [8] H. Mehrabi and H. Rahimpour-Bonab, "Paleoclimate and tectonic controls on the depositional and diagenetic history of the Cenomanian-early Turonian carbonate reservoirs, Dezful Embayment, SW Iran," *Facies*, vol. 60, no. 1, pp. 147-167, 2014.
- [9] L. Chou, R. M. Garrels, and R. Wollast, "Comparative study of the kinetics and mechanisms of dissolution of carbonate minerals," *Chemical Geology*, vol. 78, no. 3-4, pp. 269-282, 1989.
- [10] G. Kaufmann and W. Dreybrodt, "Calcite dissolution kinetics in the system $CaCO_3-H_2O-CO_2$ at high undersaturation," *Geochimica et Cosmochimica Acta*, vol. 71, no. 6, pp. 1398-1410, 2007.
- [11] J. W. Morse and R. S. Arvidson, "The dissolution kinetics of major sedimentary carbonate minerals," *Earth-Science Reviews*, vol. 58, no. 1-2, pp. 51-84, 2002.
- [12] L. N. Plummer, T. M. L. Wigley, and D. L. Parkhurst, "The kinetics of calcite dissolution in CO_2 -water systems at 5 degrees to 60 degrees C and 0.0 to 1.0 atm CO_2 ," *American Journal of Science*, vol. 278, no. 2, pp. 179-216, 1978.
- [13] O. S. Pokrovsky, S. V. Golubev, J. Schott, and A. Castillo, "Calcite, dolomite and magnesite dissolution kinetics in aqueous solutions at acid to circumneutral pH, 25 to 150 °C and 1 to 55 atm pCO_2 : new constraints on CO_2 sequestration in

- sedimentary basins,” *Chemical Geology*, vol. 265, no. 1-2, pp. 20–32, 2009.
- [14] D. Rickard and E. L. Sjöberg, “Mixed kinetic control of calcite dissolution rates,” *American Journal of Science*, vol. 283, no. 8, pp. 815–830, 1983.
- [15] J. Schott, S. Brantley, D. Crerar, C. Guy, M. Borcsik, and C. Willaime, “Dissolution kinetics of strained calcite,” *Geochimica et Cosmochimica Acta*, vol. 53, no. 2, pp. 373–382, 1989.
- [16] R. Shiraki, P. A. Rock, and W. H. Casey, “Dissolution kinetics of calcite in 0.1 M NaCl solution at room temperature: an atomic force microscopic (AFM) study,” *Aquatic Geochemistry*, vol. 6, no. 1, pp. 87–108, 2000.
- [17] W. B. Durham, W. L. Bourcier, and E. A. Burton, “Direct observation of reactive flow in a single fracture,” *Water Resources Research*, vol. 37, no. 1, pp. 1–12, 2001.
- [18] R. L. Detwiler, “Experimental observations of deformation caused by mineral dissolution in variable-aperture fractures,” *Journal of Geophysical Research: Solid Earth*, vol. 113, no. B8, 2008.
- [19] J. W. Morse, R. S. Arvidson, and A. Lüttge, “Calcium carbonate formation and dissolution,” *Chemical Reviews*, vol. 107, no. 2, pp. 342–381, 2007.
- [20] J. Kirstein, H. Hellevang, B. G. Haile, G. Gleixner, and R. Gaupp, “Experimental determination of natural carbonate rock dissolution rates with a focus on temperature dependency,” *Geomorphology*, vol. 261, pp. 30–40, 2016.
- [21] Z. Li, J. Gao, W. Li, J. Wu, C. Liu, and Y. Ma, “The characteristics of geothermal field and controlling factors in Qaidam Basin, Northwest China,” *Earth Science Frontiers*, vol. 23, no. 5, 2016.
- [22] W. Liu, C. Liu, Y. Ma et al., “A study of the Lower Paleozoic accumulation condition in Delingha region in Qaidam Basin,” *Earth Science Frontiers*, vol. 23, no. 5, pp. 119–126, 2016.
- [23] Y. Yang, Y. Ma, C. Liu, H. Cheng, and Z. Li, “Influence of weathering on abundance of source rocks: a case study of Keluke Formation of Upper Carboniferous in the Shihuigou area, North Margin of Qaidam Basin,” *Earth Science Frontiers*, vol. 23, no. 5, pp. 113–118, 2016.
- [24] C. Noiriel, P. Gouze, and B. Madé, “3D analysis of geometry and flow changes in a limestone fracture during dissolution,” *Journal of Hydrology*, vol. 486, pp. 211–223, 2013.
- [25] P. Cao, Z. T. Karpyn, and L. Li, “Self-healing of cement fractures under dynamic flow of CO₂-rich brine,” *Water Resources Research*, vol. 51, no. 6, pp. 4684–4701, 2015.
- [26] J. E. Elkhoury, P. Ameli, and R. L. Detwiler, “Dissolution and deformation in fractured carbonates caused by flow of CO₂-rich brine under reservoir conditions,” *International Journal of Greenhouse Gas Control*, vol. 16, Supplement 1, pp. S203–S215, 2013.
- [27] M. Garcia-Rios, L. Luquot, J. M. Soler, and J. Cama, “Influence of the flow rate on dissolution and precipitation features during percolation of CO₂-rich sulfate solutions through fractured limestone samples,” *Chemical Geology*, vol. 414, pp. 95–108, 2015.
- [28] P. Szymczak and A. J. C. Ladd, “Wormhole formation in dissolving fractures,” *Journal of Geophysical Research*, vol. 114, no. B6, 2009.
- [29] R. L. Detwiler, R. J. Glass, and W. L. Bourcier, “Experimental observations of fracture dissolution: the role of Peclet number on evolving aperture variability,” *Geophysical Research Letters*, vol. 30, no. 12, 2003.
- [30] P. E. Dijk, B. Berkowitz, and Y. Yechieli, “Measurement and analysis of dissolution patterns in rock fractures,” *Water Resources Research*, vol. 38, no. 2, pp. 5-1–5-12, 2002.
- [31] P. Gouze, C. Noiriel, C. Bruderer, D. Loggia, and R. Leprovost, “X-ray tomography characterization of fracture surfaces during dissolution,” *Geophysical Research Letters*, vol. 30, no. 5, 2003.
- [32] A. Polak, D. Elsworth, J. Liu, and A. S. Grader, “Spontaneous switching of permeability changes in a limestone fracture with net dissolution,” *Water Resources Research*, vol. 40, no. 3, 2004.
- [33] W. Dreybrodt and D. Buhmann, “A mass transfer model for dissolution and precipitation of calcite from solutions in turbulent motion,” *Chemical Geology*, vol. 90, no. 1-2, pp. 107–122, 1991.
- [34] Z. Liu and W. Dreybrodt, “Dissolution kinetics of calcite in CO₂-H₂O solutions in turbulent flow: the role of the diffusion boundary layer and the slow reaction CO₂+H₂O=H⁺+HCO₃⁻,” *Acta Geologica Sinica*, vol. 72, no. 4, pp. 340–348, 1998.
- [35] A. Chaudhuri, H. Rajaram, and H. Viswanathan, “Alteration of fractures by precipitation and dissolution in gradient reaction environments: computational results and stochastic analysis,” *Water Resources Research*, vol. 44, no. 10, 2008.
- [36] P. Dijk and B. Berkowitz, “Precipitation and dissolution of reactive solutes in fractures,” *Water Resources Research*, vol. 34, no. 3, pp. 457–470, 1998.
- [37] T. Min, Y. Gao, L. Chen, Q. Kang, and W. Tao, “Changes in porosity, permeability and surface area during rock dissolution: effects of mineralogical heterogeneity,” *International Journal of Heat and Mass Transfer*, vol. 103, pp. 900–913, 2016.
- [38] J. L. Huit, “Fluid flow in simulated fractures,” *AIChE Journal*, vol. 2, no. 2, pp. 259–264, 1956.
- [39] P. A. Witherspoon, J. S. Y. Wang, K. Iwai, and J. E. Gale, “Validity of cubic law for fluid flow in a deformable rock fracture,” *Water Resources Research*, vol. 16, no. 6, pp. 1016–1024, 1980.
- [40] W. Dreybrodt, “Mixing corrosion in CaCO₃/1bCO₂/1bH₂O systems and its role in the karstification of limestone areas,” *Chemical Geology*, vol. 32, no. 1-4, pp. 221–236, 1981.
- [41] W. Dreybrodt, J. Lauckner, L. Zaihua, U. Svensson, and D. Buhmann, “The kinetics of the reaction CO₂ + H₂O → H⁺ + HCO₃⁻ as one of the rate limiting steps for the dissolution of calcite in the system H₂O-CO₂-CaCO₃,” *Geochimica et Cosmochimica Acta*, vol. 60, no. 18, pp. 3375–3381, 1996.
- [42] Z. Liu and W. Dreybrodt, “Dissolution kinetics of calcium carbonate minerals in H₂O-CO₂ solutions in turbulent flow: The role of the diffusion boundary layer and the slow reaction H₂O + CO₂ → H⁺ + HCO₃⁻,” *Geochimica et Cosmochimica Acta*, vol. 61, no. 14, pp. 2879–2889, 1997.
- [43] Z. Liu and D. Wolfgang, “Kinetics and rate-limiting mechanisms of dolomite dissolution at various CO₂ partial pressures,” *Science in China Series B: Chemistry*, vol. 44, no. 5, pp. 500–509, 2001.
- [44] U. Svensson and W. Dreybrodt, “Dissolution kinetics of natural calcite minerals in CO₂-water systems approaching calcite equilibrium,” *Chemical Geology*, vol. 100, no. 1-2, pp. 129–145, 1992.
- [45] L. N. Plummer and E. Busenberg, “The solubilities of calcite, aragonite and vaterite in CO₂-H₂O solutions between 0 and 90°C, and an evaluation of the aqueous model for the system

- CaCO₃-CO₂-H₂O,” *Geochimica et Cosmochimica Acta*, vol. 46, no. 6, pp. 1011–1040, 1982.
- [46] Z. Liu, W. Drebrodt, J. Han, and H. Li, “Equilibrium chemistry of the CaCO₃-CO₂-H₂O system and discussions,” *Carsologica Sinica*, vol. 24, pp. 1–14, 2005.
- [47] X. You, X. Zhang, and X. You, “Simulation on an aqueous solution of calcium carbonate,” *Journal of Huazhong Normal University*, vol. 46, no. 6, pp. 686–689, 2012.
- [48] R. L. Detwiler and H. Rajaram, “Predicting dissolution patterns in variable aperture fractures: evaluation of an enhanced depth-averaged computational model,” *Water Resources Research*, vol. 43, no. 4, 2007.
- [49] F. Golfier, C. Zarcone, B. Bazin, R. Lenormand, D. Lasseux, and M. Quintard, “On the ability of a Darcy-scale model to capture wormhole formation during the dissolution of a porous medium,” *Journal of Fluid Mechanics*, vol. 457, pp. 213–254, 2002.
- [50] N. Kalia and V. Balakotaiah, “Effect of medium heterogeneities on reactive dissolution of carbonates,” *Chemical Engineering Science*, vol. 64, no. 2, pp. 376–390, 2009.
- [51] A. C. Lasaga, “Chemical kinetics of water-rock interactions,” *Journal of Geophysical Research*, vol. 89, no. B6, pp. 4009–4025, 1984.
- [52] P. Szymczak and A. J. C. Ladd, “The initial stages of cave formation: beyond the one-dimensional paradigm,” *Earth and Planetary Science Letters*, vol. 301, no. 3–4, pp. 424–432, 2011.
- [53] A. C. Lasaga, *Kinetic Theory in the Earth Sciences*, Princeton University Press, Princeton, NJ, USA, 1998.
- [54] C. N. Fredd and H. S. Fogler, “Influence of transport and reaction on wormhole formation in porous media,” *AIChE Journal*, vol. 44, no. 9, pp. 1933–1949, 1998.
- [55] A. M. Tartakovsky, P. Meakin, T. D. Scheibe, and B. D. Wood, “A smoothed particle hydrodynamics model for reactive transport and mineral precipitation in porous and fractured porous media,” *Water Resources Research*, vol. 43, no. 5, 2007.
- [56] P. C. Lichtner and Q. Kang, “Upscaling pore-scale reactive transport equations using a multiscale continuum formulation,” *Water Resources Research*, vol. 43, no. 12, 2007.



Hindawi

Submit your manuscripts at
www.hindawi.com

